JMEPEG (2023) 32:8337–8345
https://doi.org/10.1007/s11665-022-07699-z

1059-9495/$19.00

TECHNICAL ARTICLE

Corrosion Behavior of High Strength Steel Welded Joint in Seawater: A Combinatorial Study Based on General and Localized Electrochemical Methods

Xuehui Liu, Yongqiang Sui, Huixia Zhang, Likun Xu, Hongtao Tong, and Hongqing Song

Submitted: 8 August 2022 / Revised: 21 October 2022 / Accepted: 19 November 2022 / Published online: 5 December 2022

In the present work, the corrosion behavior of ultra-high strength steel (UHSS)-high strength steel (HSS) welded joint is investigated. In situ scanning Kelvin probe (SKP) and scanning vibrating electrode technique (SVET) are used to study the galvanic corrosion of the dissimilar welded joint in natural seawater medium. The UHSS zone is revealed to be the most cathodic region. Meanwhile, the HSS has a high anodic activity. The corroded surface shows that the calcareous deposit is observed in UHSS zone, and the rust layer is formed in HSS and weld metal (WM) zones. When the corrosion product layer is removed, the UHSS zone is revealed to suffer from the pitting corrosion, and the HSS and WM zones exhibit the uniform corrosion.

Keywords dissimilar joints, galvanic effect, high strength steel, scanning Kelvin probe (SKP), scanning vibrating electrode technique (SVET)

1. Introduction

High strength steel (HSS) materials have been widely used in the automotive, bridge, marine transportation and petrochemical industries due to their excellent mechanical properties (Ref 1, 2). To expand the application of HSS alloys and improve their design flexibility in the ocean engineering and shipbuilding industry, the welding among dissimilar steels is indispensable (Ref 3). In recent years, the excellent mechanical property of HSS welded joint has received extensive attention. However, rare research on its corrosion problems can be found, especially for the welding joint used in many industries such as oil and shipbuilding (Ref 4, 5).

The corrosion decreases the mechanical property of the welded joints, so that this problem has to be seriously considered for its application. Abioye et al. investigated the effect of welding speed on corrosion behavior of the dissimilar welded joint of stainless steel and low carbon steel, and the corrosion performance was found to improve as the welding speed decreased (Ref 6). Huang et al. studied the effect of heat input on corrosion behavior of dissimilar welded joint and recommended a higher heat input to improve its corrosion resistance (Ref 7). Due to the difference in chemical and metallurgical change in the welding process, the coupling of two different steels may also lead to increased susceptibility to localized galvanic corrosion (Ref 8). Wint et al. investigated the local corrosion behavior of the dissimilar joint in 0.017 M NaCl. The dissimilar joint exhibited the corrosion centered on the UHSS part (Ref 9). Huang et al. discovered that the difference in microstructure and chemical composition resulted in various galvanic effect of the HSS welded joint (Ref 10). Although several factors (e. g., heat input, welding speed and the chemical composition of the steel) have been studied to influence the corrosion of the dissimilar welded joint, there is still little research on the UHSS coupled to HSS.

The aim of the present work is to study the corrosion behavior of the UHSS- HSS welded joint in corrosive environment. The potentiodynamic polarization and electrochemical impedance spectroscopy (EIS) were used as electrochemical tools to study the welded joint. A combination of the scanning vibrating electrode technique (SVET) and scanning Kelvin probe (SKP) were employed to investigate the galvanic effect between the UHSS and HSS from the localized perspective. The morphology and composition of the corrosion products formed on welded joint surface after immersion test were revealed by SEM coupled with energy-dispersive spectroscopy (EDS).

2. Experimental Procedures

2.1 Materials

In this study, the UHSS and HSS sheets were used as the base metals, which were supplied by ANGANG STEEL Co., Ltd. (China). The yield strength of UHSS and HSS were 1049 and 672 MPa, respectively. The chemical composition of both steels is given in Table 1.

The UHSS-HSS weld joints were produced by manual welding process. The main parameters of manual welding process were 170 A welding current, 30 V welding voltage and

Xuehui Liu, Yongqiang Sui, Huixia Zhang, Likun Xu, Hongtao Tong, and **Hongqing Song**, State Key Laboratory for Marine Corrosion and Protection, Luoyang Ship Material Institute, 37 Wenhai Middle Road, Qingdao 266237 Shandong, China. Contact e-mail: xhliu68@126.com.

Table 1 The chemical composition (wt.%) of UHSS and HSS steels

Elements	C	Si	Mn	P	S	Ni	Cr	Mo	V	Fe
UHSS	0.092	0.36	0.63	0.008	0.003	9.4	0.62	0.95	0.10	Bal
HSS	0.089	0.28	0.44	0.0075	0.0022	3.73	1.13	0.42	0.66	Bal

16 kJ/cm heating input. The test samples were cut from the middle part of the welded joints with a dimension of 90 × 30 × 3 mm.

2.2 Characterization

In order to observe the microstructure of the welded joint, the samples were grounded with silicon carbide paper up to 2400 grit under wet condition. Then, they were roughly polished with 2.5 μm diamond paste. Finally, they were polished with 1 μm diamond paste. After that, the specimens were etched with 4% nital solution (4 mL nitric acid + 96 mL ethyl alcohol). The microstructures of different zones were characterized using Zeiss Axio Observer Z1m optical microscope. Scanning electron microscopy (SEM, ZEISS ULTRA 55) coupled with EDS was used to survey the microstructure and the rust film on different zone of welded joint. The rust layer was removed from the corroded zone and subjected to spectroscopic analysis (Raman). Raman test was carried out using a Horiba LabRAM HR Evolution instrument with wavelength of 532 nm. The scanning range was fixed as 100-1600 cm^{-1}.

2.3 Conventional Electrochemical Corrosion Tests

The surface of welded joint was mechanically ground sequentially to 2000 grit with silicon carbide paper and then diamond paste. After the polishing, they were rinsed with deionized water and absolute ethyl alcohol. Then they were dried by cold air. Except an exposed surface of 1 cm^2, the rest of the surface was sealed with organic silicone sealant. The test was conducted in natural seawater collected from Aoshan Bay, Qingdao, China. The electrochemical tests were carried out on a VMP3 BioLogic electrochemical workstation in a three-electrode configuration at room temperature. The sample acted as working electrode (WE). A saturated calomel electrode (SCE) was reference electrode (RE), and a platinum sheet was counter electrode (CE). Before the experiment, the specimen was exposure to seawater for 1 h to keep the surface stability. The potentiodynamic polarization tests were conducted from − 0.25 to 0.25 V (versus E_{corr}, corrosion potential) at a rate of 0.167 mV/s. The EIS measurements were performed at open circuit potential (OCP) after 1 h OCP test for achieving a stable state, and the frequency range was set from 10 mHz to 100 kHz with a 10 mV sinusoidal amplitude. The EIS data were fitted by ZSimpWin software. For EIS and polarization measurements, three trials were carried out to ensure the repeatability.

2.4 SKP Measurements

SKP potential maps were obtained using a Princeton VersaSCAN scanning electrochemical workstation. The probe was set to vibrate perpendicularly to the specimen surface at a frequency of 80 Hz with an amplitude of 30 μm. The mean distance between the probe tip and the sample surface was controlled at 100 μm. The working model of SKP was a step scan, by which the Kelvin probe was stepped over a designated area of the welded joint. The probe for knowing the potential was a tungsten wire with diameter of 500 μm, and the scanning speed was set as 500 μm/s.

2.5 SVET Measurements

The SVET measurements were carried out on a Princeton VersaSCAN electrochemical workstation. A Pt-Ir electrode probe (d = 10 μm) was placed on the assigned surface at a distance of about 100 μm. The vibrating amplitude of the micro-electrode was 30 μm, and the vibrating frequency was 80 Hz. When the microelectrode was located at the vibrating peak and valley, the potential difference (ΔE) was measured. The potential was detected on an area of 40 × 4 mm with a scanning rate of 500 μm/s. The current density in solution can be calculated using the following equation (Ref 11):

$$j = -\sigma \frac{\Delta E}{A} \quad \text{(Eq 1)}$$

where j is the current density (A m^{-2}), σ is the conductivity of the seawater solution (5.6 S m^{-1}), ΔE is the measured potential difference (V), and A is the vibration amplitude adopted in the experiment.

3. Results and Discussion

3.1 The Microstructure of UHSS-UHSS Welded Joint

The microstructures of UHSS and HSS are shown in Fig. 1. It is observed that the microstructure of UHSS and HSS is relatively uniform tempered sorbite, for which fine granular cementite evenly distributes in the equiaxed ferrite (Ref 12). In Fig. 2, the microstructure of the heat affected zone (HAZ) and weld metal is demonstrated. The WM mainly consists of granular bainite with a few acicular ferrites. The HAZ at UHSS side shows bainitic microstructure. For HAZ at HSS side, it displays a microstructure with granular bainite and troostite.

3.2 Electrochemical Measurements

Figure 3 shows the potentiodynamic polarization curves of the UHSS, WM and HSS zones of the welded joint in natural seawater solution. From the curves, all the test samples exhibit an active response, suggesting the poor protection behavior of oxide film against corrosion. The corrosion kinetic parameters including corrosion potential (E_{corr}) and corrosion current density (I_{corr}) are evaluated by the Tafel linear extrapolation method (Ref 13), as shown in Table 2. The corrosion potential is found to have a small difference between UHSS and HSS, but the corrosion current density is respectively about the scale of 10^{-6} and 10^{-5} A /cm^2 for the UHSS and HSS, which shows that the UHSS has better corrosion resistance. This may

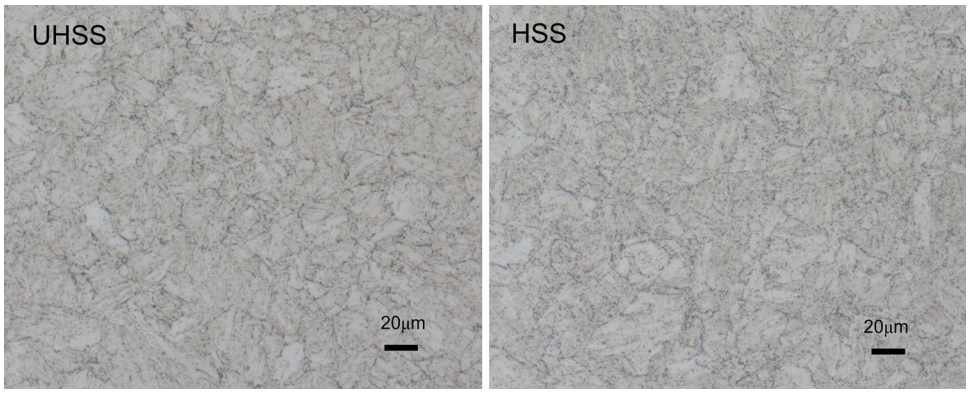

Fig. 1 Microstructure of the UHSS and HSS, which was etched by 4% nitric acid-alcohol solution

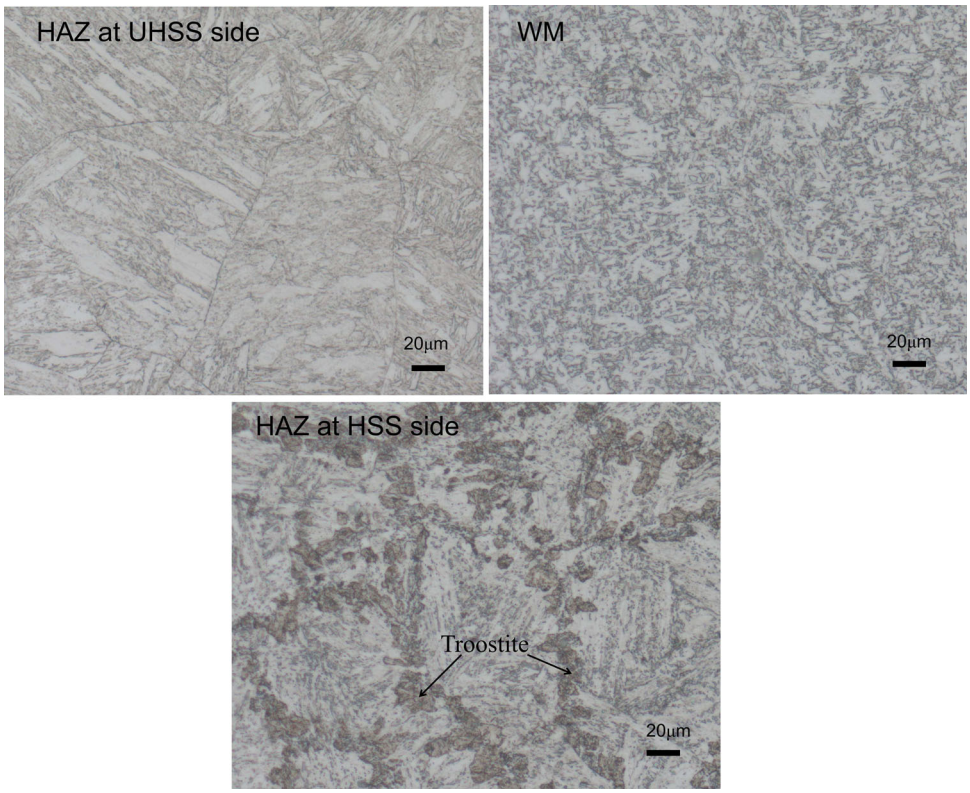

Fig. 2 Microstructure of HAZ at the UHSS side, WM and HAZ at the HSS side

be due to the higher Ni content (9.4%) in the UHSS compared with the HSS (3.73%), which provides a possibility for improving the corrosion resistance (Ref 14). Test results show that in the welded joint, the UHSS is less susceptible to be corroded. Moreover, there is little difference between HSS and WM on the corrosion resistance.

EIS measurement is performed to further investigate the corrosion resistance of UHSS, WM and HSS. Figure 4 shows the Bode and Nyquist plots of UHSS, HSS and WM after exposure to natural seawater. The Z' is the real part of the total complex impedance, the Z'' is the imaginary part of the total complex impedance, and the $|Z|$ is the total complex impedance. Figure 4(a) shows that the Nyquist plots of UHSS and HSS are all flat capacitive arcs, the larger diameter of which implies the larger charge transfer resistance and the better corrosion resistance (Ref 7). For WM, the Nyquist impedance plot consists of a capacitive arc at high frequency and an inductive loop at low frequency. The capacitive arc is attributed to the charge-transfer process, and the inductive loop is caused by the absorption/desorption of the intermediate species formed during the charge transfer process (Ref 6). From the Bode $-|Z|$ results shown in Fig. 4(b), it can be observed that the $|Z|$ value of HSS and WM is approximately similar, which is lower than that of the UHSS. Thus, the corrosion resistance of the UHSS is the best.

Suitable electrical equivalent circuits (EEC) shown in Fig. 5 are used to fit the EIS data. For the equivalent circuit, R_f and C_f are respectively associated with the resistance and capacitance of the oxide film (corrosion product layer); R_{ct} and CPE_{dl} are corresponding to the charge transfer resistance and the double layer capacitance (Ref 15). For WM, the inductive element is incorporated into the EEC (Fig. 5b), considering the inductive

behavior observed at the low frequency. R_L is the inductive resistance and L is the inductance (Ref 16). CPE is a constant phase element, which is employed to replace pure capacitance, since the phase angle is not equal to − 90° (Ref 17). The impedance of CPE is expressed as: $Z_{CPE} = (Y)^{-1}(j\omega)^{-n}$, where Y is the admittance in $S\ cm^{-2}\ s^{1-n}$, ω is the frequency in rad s^{-1}; $j^2 = (-1)$, and n is the CPE power (Ref 18). The EIS parameters based on the EEC are listed in Table 3 with χ^2 value ranging from 2×10^{-3} to 5×10^{-3}. In general, R_{ct} reflects the kinetics of electrochemical reaction at metal/solution interface, and a high R_{ct} value denotes a low corrosion rate (Ref 19). In Table 3, it can be found that the UHSS shows the highest R_{ct} among the three zones, which is in accordance with the lower value of current density obtained from polarization curve results.

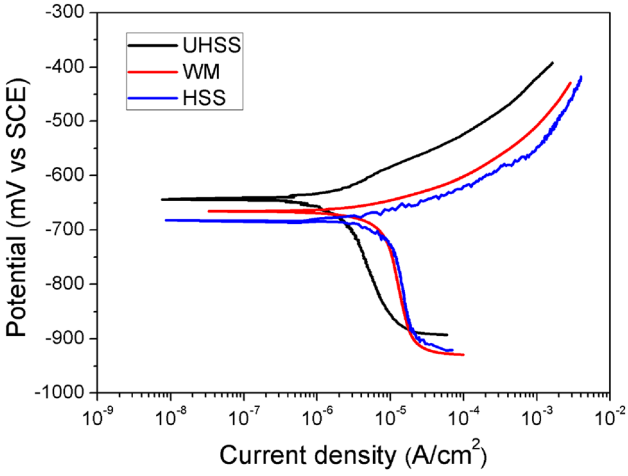

Fig. 3 Potentiodynamic polarization curves of UHSS, WM and HSS

Table 2 Electrochemical data of the UHSS, WM and HSS obtained from potentiodynamic polarization curves in natural seawater environment

Region	E_{corr}, V vesus SCE	I_{corr}, A/cm²
UHSS	− 0.641	1.53×10^{-6}
WM	− 0.664	1.22×10^{-5}
HSS	− 0.682	1.25×10^{-5}

3.3 SKP Measurement

Compared with the traditional EIS technology, the SKP technology allows in situ measurement of Volta potential variation over the metal surface (Ref 20, 21). In principle, the Kelvin probe with a fine tip measures the work function of a sample using the vibrating method. The work function of the sample can be determined by measuring the Volta potential difference between the sample and the reference electrode. It has been proved that the measured Volta potential difference linearly changes with the corrosion potential by rigorous calibration routine (Ref 22). The decrease in the work function

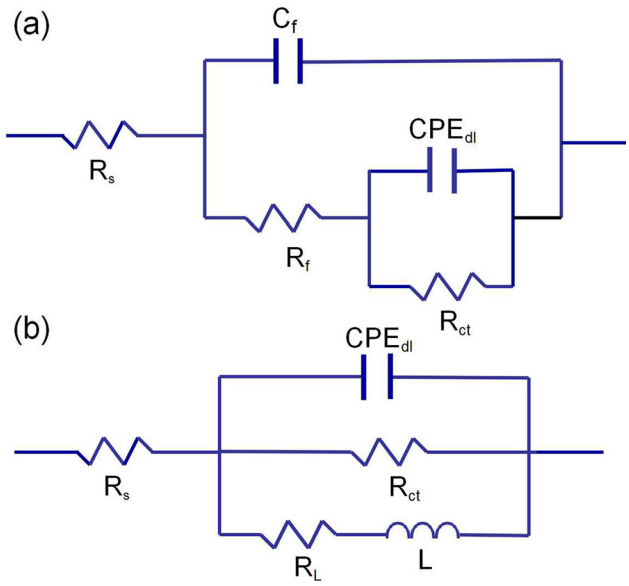

Fig. 5 Electrical equivalent circuits used to fit EIS data

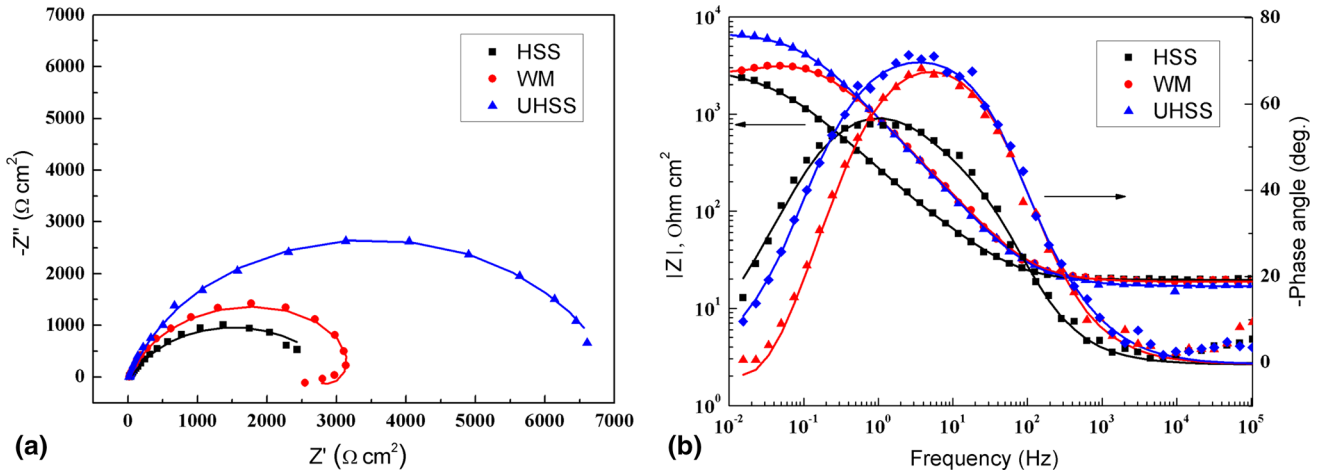

Fig. 4 Nyquist (a) and Bode plots (b) of the HSS, WM and UHSS after exposure to natural seawater

Table 3 EIS fitting parameters from equivalent circuits corresponding to HSS, WM and UHSS

specimen	R_f, Ω cm^2	C_f Y_0, Ω^{-1} s^n cm^{-2}	n_f	R_{ct}, Ω cm^2	CPE$_{dl}$ Y_0 , Ω^{-1}s^n cm^{-2}	n_{ct}	L, H cm^{-2}	R_L, Ω cm^2	x^2
HSS	65.3	3.3×10^{-4}	0.88	2917	6.6×10^{-4}	0.88	…	…	0.005
WM	…	…	…	3551	2.1×10^{-4}	0.84	7.8×10^{4}	1.0×10^{4}	0.002
UHSS	68.6	2.2×10^{-4}	0.82	6875	1.3×10^{-5}	0.98	…	…	0.003

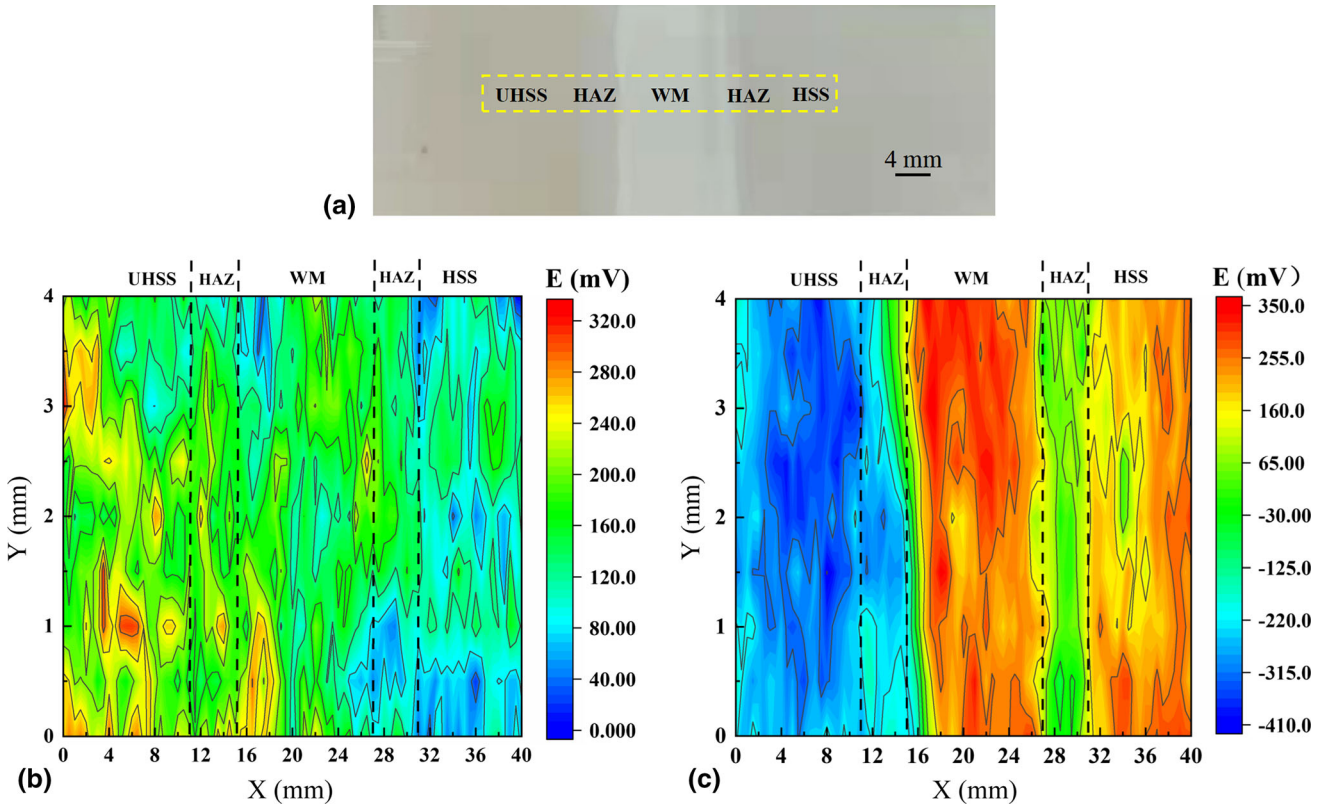

Fig. 6 (a) SKP as the tool for monitoring the potential distribution by scanning over the designated area. SKP maps of welded join before (b) and after (c) immersion in natural seawater for 72 h

or Volta potential (energy) can be considered as an increasing tendency for electron transfer. Hence, an enhanced propensity is expected to undergo electrochemical reaction (Ref 23, 24). The Kelvin probe is stepped over a designated area (40 × 4 mm) of the welded joint to obtain the potential distribution (Fig. 6). It is noticed that the potential ranges from 0 to 320 mV with maximum ΔV of 320 mV before immersion, which is higher than the critical value ($\Delta V > 200$ mV) for triggering the galvanic corrosion (Ref 25). The potential value increases in order of HSS < WM < UHSS. The UHSS having high potential acts as cathode, and HSS having low potentials acts as anode. Hence, galvanic couple is formed. The HSS zone with low potential has an increased ability to become activated state, when being exposed to the corrosive medium. After exposure to natural seawater for 72 h, the surface is mapped for the second time, and it exhibits potential value in the range of − 410 to 350 mV with maximum ΔV of 760 mV, indicating a large driving force for corrosion reaction (Ref 18). The uneven potential profile after immersion is probably due to the uneven oxide layer formed on different zones (Ref 26). This phenomenon may be attributed to the galvanic corrosion occurring on the welded joint exposure to the natural seawater.

3.4 SVET Measurement

SVET is capable of sensing anodic and cathodic processes in active sites on metal surface by using a vibrating micro-electrode (Ref 27). Figure 7 shows the SVET maps of the UHSS-HSS welded joint after different immersion time in seawater. During the initial 15 min of immersion, the anodic feature is observed at HSS zone. Meanwhile, the UHSS zone showing the cathodic feature is relatively unaffected by corrosion. After 1 h of immersion, the region of anodic attack persists, and it has grown from HSS to WM. However, the UHSS and the HAZ close to UHSS side remain completely cathodic feature (Fig. 7b). Extending the immersion time, the anodic attack initiating on the HSS has spread onto the whole welded metal, whereas the UHSS maintains relatively cathodic state. The anodic current density value of the welded sample deceases with the extending immersion time, which is ascribed to the formation of corrosion products on its surface (Ref 28, 29). The SVET results confirm that a galvanic cell is formed between HSS and UHSS, and HSS is preferentially attacked as anode.

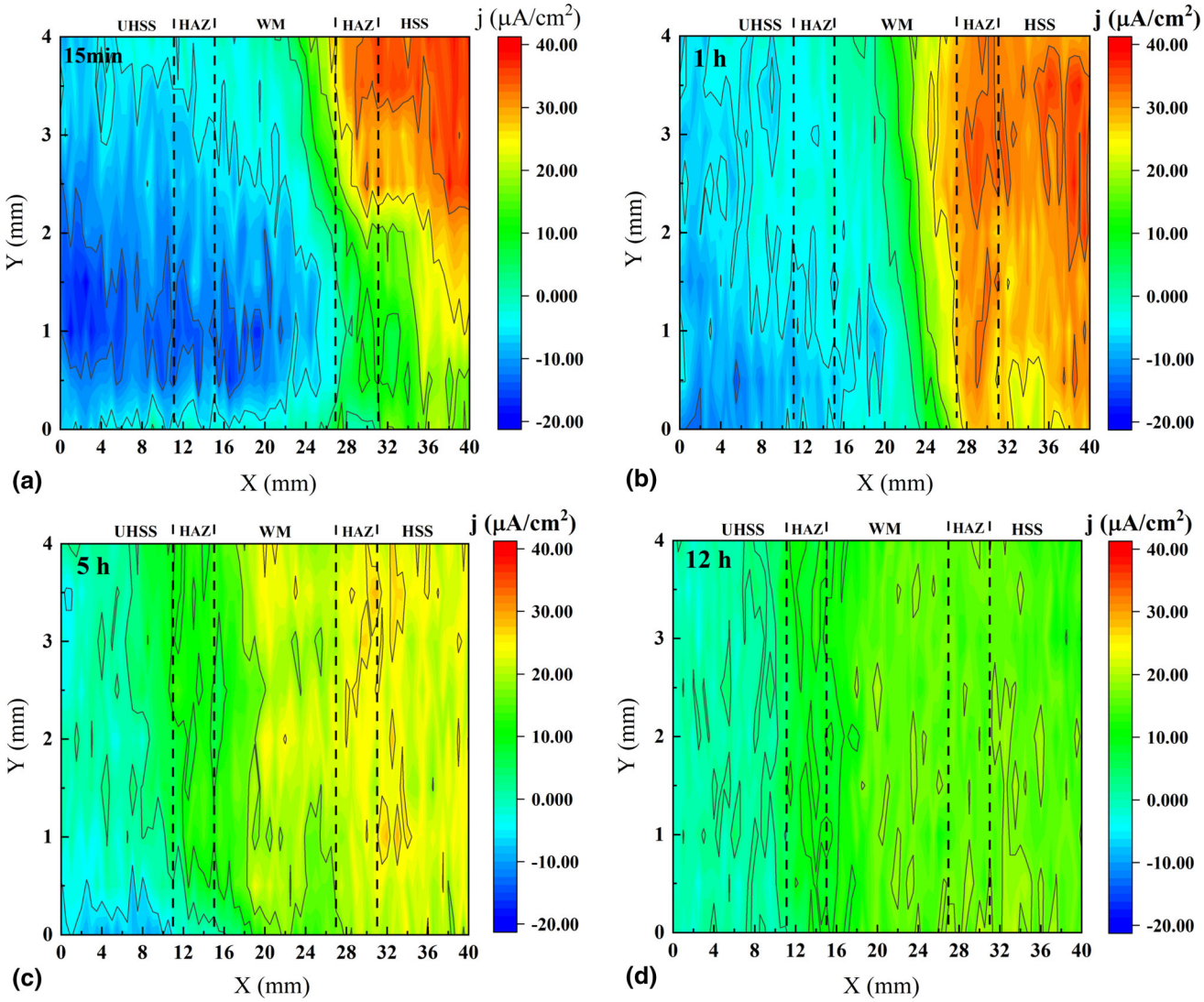

Fig. 7 SVET maps of the UHSS-HSS welded joint after different immersion time in natural seawater

3.5 Corroded Surface Characterization

The microscopic morphology of the corrosion product on welded joint after 72 h exposure to seawater solution is shown in Fig. 8. It can be found that there is some difference in the appearance of different zone. From the SEM images, the bouquet-shaped deposits are sparsely distributing on the surface of UHSS and the HAZ near to UHSS part, whose morphology is in accordance with calcareous deposit (Ref 30). The rust layer formed on HSS, HAZ near to HSS part and WM zone exhibits two kinds of morphology, such as flaky structure and flocculent morphology. The EDS tests are conducted to analyze the composition of corrosion product formed on the welded joint after immersion. For UHSS and HAZ near to UHSS, the Ca element weight contents (14.82 and 12.47 wt.%) are much higher than those of other zones, indicating the calcareous deposit formation due to the cathodic reaction. For the zones from HSS to WM, the corrosion product is mainly composed of iron oxide due to the reaction between metal and oxygen. The results of surface characterization confirm that the galvanic corrosion occurs on the UHSS-HSS welded joint after immersion in seawater, which properly matches the SVET results. It is worth to note that the corrosion extension of various region on the welded joints is not only dependent on the galvanic effect but also on the Ni/Fe ratio in the corrosion product. Generally, enriching of Ni element in the corrosion layer can block the introduction of Cl^- to give a better corrosion protection for the substrate (Ref 14, 31). From the EDS results, the high Ni/Fe ration (0.071) value is observed in the corrosion product film for the UHSS, and the low value is corresponding to the HSS (0.020). Therefore, the UHSS will be better protected after the formation of the corrosion product layer.

The phase composition of the rust generated on HSS, HAZ near HSS side and WM zones was analyzed by Raman spectra, as shown in Fig. 9. It is observed that the iron oxide formed on HSS and WM zones is mainly composed of goethite (α-FeOOH) and hematite (α-Fe_2O_3). The strong peaks at 390^{-1} and 660 cm^{-1} correspond to α-FeOOH (Ref 32). The characteristic peaks of α-Fe_2O_3 are associated with the bands at 221 cm^{-1} and 285 cm^{-1} (Ref 33). The rust of HAZ near to HSS part is composed of α-FeOOH, β-FeOOH and γ-FeOOH (Ref 32). The complex mixing of different FeOOH phase generated on HAZ zone may be associated with its dual-phase structure (Ref 34).

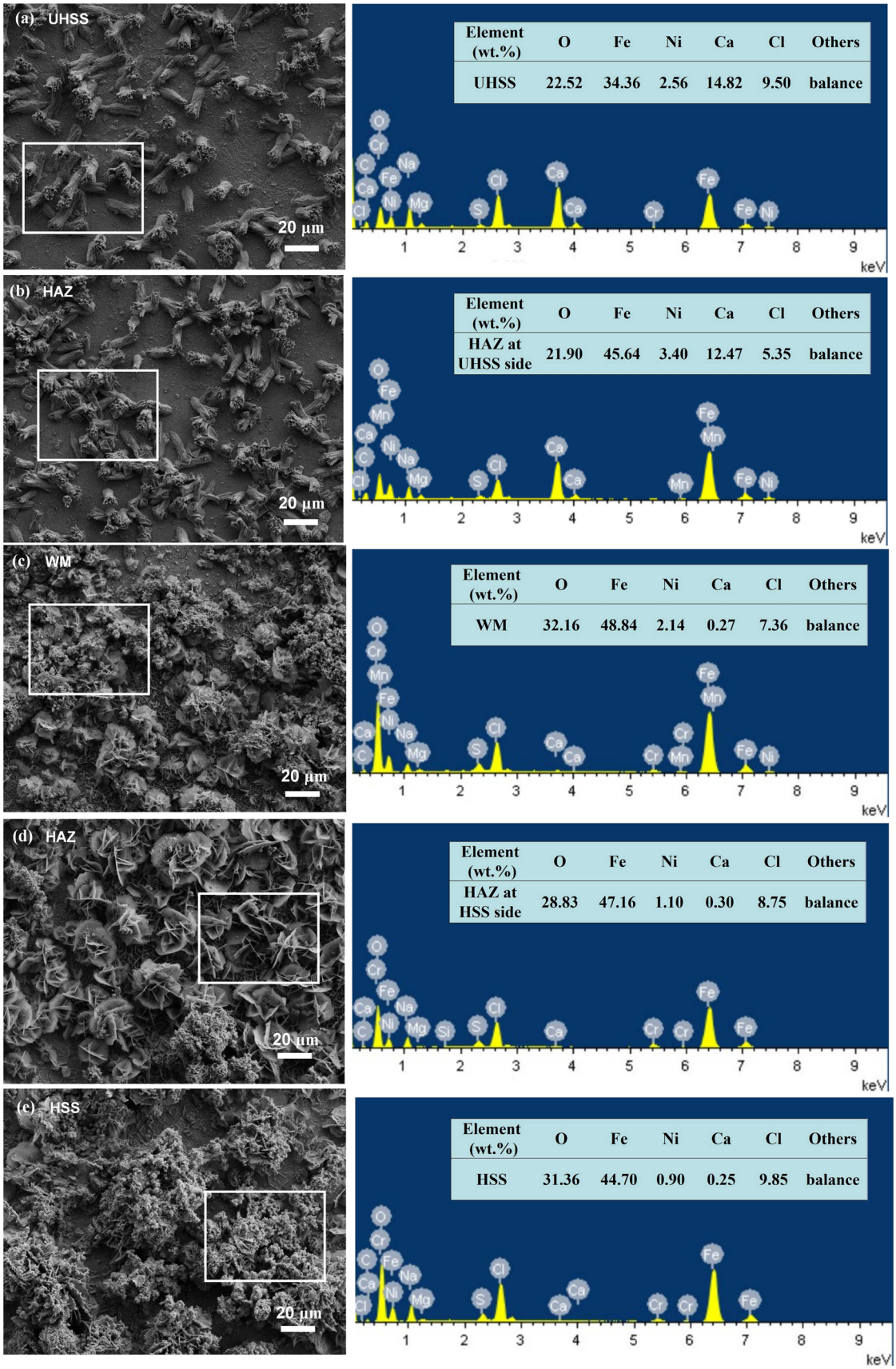

Fig. 8 SEM and EDS results of corrosion product film formed on the welded joint after 72 h exposure to seawater. (a) UHSS, (b) HAZ near UHSS part, (c) WM, (d) HAZ near HSS part, and (e) HSS. EDS corresponds to elements detected in the marked area of (a-e)

The corrosion product is assumed to form in seawater in accordance with following cathodic and anodic reactions. The main cathodic reaction is oxygen reduction as follows:

$$O_2 + 2H_2O + 4e^- \rightarrow 4OH^- \quad \text{(Eq 2)}$$

Carbonate ions are generated by the slow reaction between atmospheric carbon dioxide and water, which can be expressed as follows (Ref 35):

$$CO_2 + H_2O \rightarrow H_2CO_3 \quad \text{(Eq 3)}$$

$$H_2CO_3 \rightarrow H^+ + HCO_3^- \quad \text{(Eq 4)}$$

$$HCO_3^- \rightarrow H^+ + CO_3^{2-} \quad \text{(Eq 5)}$$

Subsequently, the formation of $CaCO_3$ will occur at cathodic sites:

$$CaSO_4 + CO_3^{2-} \rightarrow CaCO_3 + SO_4^{2-} \quad \text{(Eq 6)}$$

Iron and oxygen form a rust compound at anodic sites involving several steps (Ref 33):

$$Fe - 2e^- \rightarrow Fe^{2+} \quad \text{(Eq 7)}$$

$$Fe^{2+} + 2OH^- \rightarrow Fe(OH)_2 \quad \text{(Eq 8)}$$

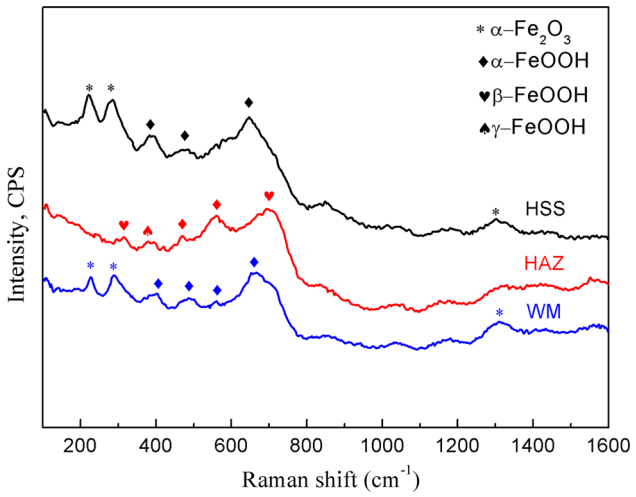

Fig. 9 Raman spectra of the rust layer generated on HSS, HAZ near to HSS part and WM zones after immersion in natural seawater for 72 h

$$4Fe(OH)_2 + O_2 + H_2O \rightarrow 4Fe(OH)_3 \quad \text{(Eq 9)}$$

$$Fe(OH)_3 \rightarrow FeOOH + H_2O \quad \text{(Eq 10)}$$

$$FeOOH + Fe^{2+} + 2e^- \rightarrow 3Fe_2O_3 + 4H_2O \quad \text{(Eq 11)}$$

Figure 10 shows the morphology of UHSS-HSS welded joint after removing the corrosion product film. The pitting corrosion is observed in the UHSS zone. The WM and HSS zones are found to dissolve in uniform corrosion. Although the UHSS has been protected by cathodic effect provided by HSS, the corrosion is found after 72 h immersion. This phenomenon illustrates that the cathodic protection against UHSS weakens with extending immersion time. This may be attributed to the formation of corrosion product on various zones, which affects the potential value of each region. And the cathodic and anodic feature on the welded joint may reverse after a long period immersion.

4. Conclusions

In this paper, the corrosion behavior of the UHSS-HSS welded joint is studied. The main findings are as follows:

(1) The corrosion behavior of welded sample is studied by EIS and polarization curve techniques. The UHSS shows the best corrosion resistance among all zones of the welded joint.
(2) SKP results indicate that the HSS zone with low potential has an increased tendency to become activated state when being exposed to the corrosive medium.
(3) SVET maps show that the localized anodic activity preferentially initiates at the HSS zone. Meanwhile, the UHSS remains completely cathodic activity at the early immersion stage.
(4) The results of surface characterization confirm that the galvanic corrosion occurs on the UHSS-HSS welded joint. The calcareous deposit is generated on UHSS zone, and the rust layer is mainly formed on HSS and WM zones. After the removal of the corrosion product, pitting corrosion is observed on UHSS surface. Meanwhile, WM and HSS are consumed in uniform corrosion.

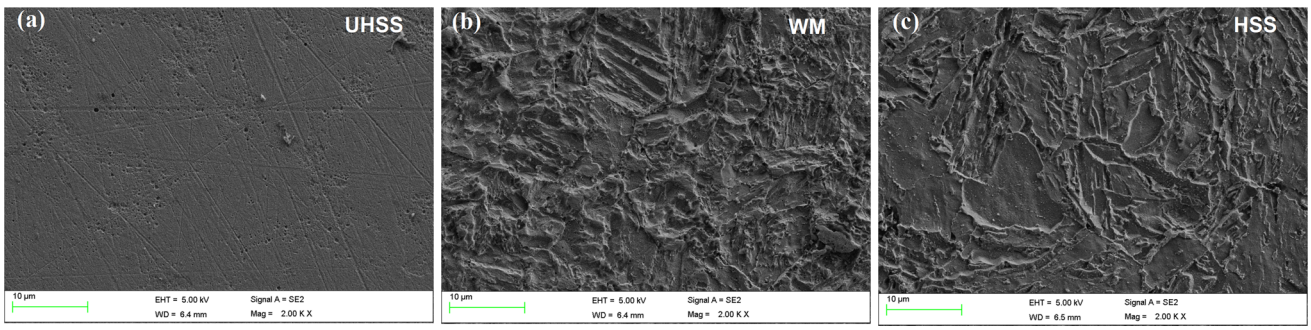

Fig. 10 SEM surface morphology of welded joint after removal of the corrosion products: (a) UHSS, (b) WM, and (c) HSS

Acknowledgments

The authors are grateful to Luoyang Ship Material Research Institute for the financial support for this research work.

Conflict of interest

No potential conflict of interest was reported by the author(s).

References

1. M.M. Ran, Z. YC, Y.Z. Wang et al., Fracture Prediction in Transverse Fillet Welded Joints of High Strength Structural Steel, *J. Constr. Steel Res.*, 2022, **189**, p 107101
2. S.K. Dwivedi and M. Vishwakarma, Effect of Hydrogen in Advanced High Strength Steel Materials, *Int. J. Hydrogen Energ.*, 2019, **44**, p 28007–28030
3. X. Lei, S. Dong, J. Huang et al., Phase Evolution and Mechanical Properties of Coarse-Grained Heat Affected Zone of a Cu-Free High Strength Low Alloy Hull Structure Steel, *Mater. Sci. Eng. A*, 2018, **718**, p 437–448
4. L. de Jorge, V.S. Cândido, A.C.R. da Silva et al., Mechanical Properties and Microstructure of SMAW Welded and Thermically Treated HSLA-80 Steel, *J. Mater Res. Technol.*, 2018, **7**, p 598–605
5. M. Dedisa, J. Michal, V. Tibor et al., Examination of Fatigue Life of HSLA Domex 700 MC Welded Joints, *Transport. Res. Procedia*, 2021, **55**, p 533–537
6. T.E. Abioye, O.E. Ariwoola, T.I. Ogedengbe et al., Effects of Welding Speed on the Microstructure and Corrosion Behavior of Dissimilar Gas Metal Arc Weld Joints of AISI 304 Stainless Steel and Low Carbon Steel, *Mater. Today Proc.*, 2019, **17**, p 871–877
7. Y. Huang, J. Huang, J. Zhang et al., Microstructure and Corrosion Characterization of Weld Metal in Stainless Steel and Low Carbon Steel Joint Under Different Heat Input, *Mater. Today Commun.*, 2021, **29**, p 102948
8. D. Liu, H. Zhao, D. Tang et al., Corrosion Behavior Study of 22MnB5 Steel and Its Weld Using Electrochemical Method, *Appl. Mech. Mater.*, 2014, **496–500**, p 340–343
9. N. Wint, J. Leung, J.H. Sullivan et al., The Galvanic Corrosion of Welded Ultra-High Strength Steels Used for Automotive Applications, *Corros. Sci.*, 2018, **136**, p 366–373
10. C. Huang, F. Huang, H.X. Liu et al., The Galvanic Effect of High-Strength Weathering Steel Welded Joints and Its Influence on Corrosion Resistance, *Corros. Eng. Sci. Tehchnol.*, 2019 https://doi.org/10.1080/1478422X.2019.1636484
11. K.B. Deshpande, Experimental Investigation of Galvanic Corrosion: Comparison Between SVET and Immersion Techniques, *Corros. Sci.*, 2010, **52**, p 2819–2826
12. C. Gao, M.Q. Yang, J.C. Pang et al., Abnormal Relation Between Tensile and Fatigue Strengths for a High-Strength Low-Alloy Steel, *Mater. Sci. Eng.*, 2022, **832**, p 142418
13. H. Tristijanto, M.N. Ilman, and P.T. Iswanto, Corrosion Inhibition of Welded of X-52 Steel Pipelines by Sodium Molybdate in 3.5% NaCl Solution, *Egypt J. Pet.*, 2020, **29**, p 155–162
14. T. Zhang, W. Liu, B. Dong et al., Investigation on the Nickel Content Design and the Corrosion Resistance of Low Alloy Steel Welded Joint in Tropical Marine Atmosphere Environment, *Mater. Corros.*, 2021, **72**, p 1620–1634
15. Y.J. Lin and C.S. Lin, Galvanic Corrosion Behavior of Friction Stir Welded AZ31B Magnesium Alloy and 6N01 Aluminum Alloy Dissimilar Joints, *Corros. Sci.*, 2021, **180**, p 109203
16. Y. Ma, H. Dong, P. Li et al., A Novel Corrosion Transformation Process in Aluminum Alloy/Galvanized Steel Welded Joint, *Corros. Sci.*, 2022, **194**, p 109936. https://doi.org/10.1016/j.corsci.2021.109936
17. G. Monrrabal, J.A. Jiménez, J. Ress et al., Corrosion Behaviour of Resistance-Spot-Welded High-Mn Austenitic TWIP Steel, *Corros. Eng. Sci. Techn.*, 2020 https://doi.org/10.1080/1478422X.2020.1806606
18. X. Liu, Z. Ma, H. Tong et al., Water-Based Epoxy Coatings with pH-Sensitive TiO_2 Containers for Active Corrosion Protection of Carbon Steel, *Corros. Eng. Sci. Techn.*, 2020, **55**, p 645–654
19. X. Liu, D. Zhang, P. Hou et al., Preparation and Characterization of Polyelectrolyte-Modified Attapulgite as Nanocontainers for Protection of Carbon Steel, *Electrochem. Soc.*, 2018, **165**, p C907–C915
20. S. Fajardo, A. Sánchez-Deza, M. Criado et al., Corrosion of Steel Embedded in Fly Ash Mortar Using a Transmission Line Model, *J. Electrochem. Soc.*, 2014, **161**, p E3158–E3164
21. S. Wang, Y. Li, B. Chen et al., Novel Surfactants as Green Corrosion Inhibitors for Mild Steel in 15% HCl: Experimental and Theoretical Studies, *Chem. Eng. J.*, 2020, **402**, p 126219. https://doi.org/10.1016/j.cej.2020.126219
22. J.M. Vega, S. Chimenti, and E. García-Lecina, Impact of the In-Situ Phosphatization on the Corrosion Resistance of Steel Coated with Fluorinated Waterborne Binders Assessed by SKP and EIS, *Prog. Org. Coat.*, 2020, **148**, p 105706. https://doi.org/10.1016/j.porgcoat.2020.105706
23. M. Stratmann and H. Streckel, On the Atmospheric Corrosion of Metals Which are Covered with Thin Electrolyte Layers—II, *Experimental Results. Corros. Sci.*, 1990, **30**(6), p 697–714
24. J. Li, H. Li, Y. Liang et al., Effects of Heat Input and Cooling Rate During Welding on Intergranular Corrosion Behavior of High Nitrogen Austenitic Stainless Steel Welded Joints, *Corros. Sci.*, 2020, **166**, p 108445. https://doi.org/10.1016/j.corsci.2020.108445
25. C. Örnek, C. Leygraf, and J. Pan, On the Volta Potential Measured by SKPFM Fundamental and Practical Aspects with Relevance to Corrosion Science, *Corros. Eng. Sci. Techn.*, 2019, **54**, p 185–198
26. G. Bäck, A. Nazarov, and D. Thierry, Localized Corrosion of Heat–Treated and Welded Stainless Steel Studied by Scanning Kelvin Probe, *Corros. NACA*, 2005, **61**, p 951–960
27. A.I. Ikeuba, B. Zhang, J. Wang et al., Understanding the Galvanic Corrosion of the Q-Phase/Al Couple Using SVET and SIET, *J. Mater. Sci. Techn.*, 2019, **35**, p 1444–1454
28. C. Huang, F. Huang, H.X. Liu et al., The Galvanic Effect of High-Strength Weathering Steel Welded Joints and Its Influence on Corrosion Resistance, *Corros. Eng. Sci. Techn.*, 2019, **54**, p 556–566
29. S. Wen, G. Liu, L. Wang et al., A Mathematical Model for Modeling the Formation of Calcareous Deposits on Cathodically Protected Steel in Seawater, *Electrochim. Acta.*, 2012, **78**(9), p 597–608
30. Y. Xing, Y. Sun, X. Wang et al., Effect of Surface Calcareous Deposits on Hydrogen Uptake of X80 Steel Under Strong Cathodic Current, *Int. J. Hydrogen Energ.*, 2021, **46**, p 4555–4566
31 E. Basilico, S. Marcelin, R. Mingant et al., The Effect of Chemical Species on the Electrochemical Reactions and Corrosion Product Layer of Carbon Steel in CO_2 Aqueous Environment: A Review, *Mater. Corros.*, 2021, **72**, p 1152–1167
32. W. Wei, K. Wu, X. Zhang et al., In-Situ Characterization of Initial Marine Corrosion Induced by Rare-Earth Elements Modified Inclusions in Zr-Ti Deoxidized Low-Alloy Steels, *J. Mater. Res. Technol.*, 2020, **9**, p 1412–1424
33. Y. Li, Z. Liu, E. Fan et al., The Effect of Crack tip Environment on Crack Growth Behaviour of a Low Alloy Steel at Cathodic Potentials in Artificial Seawater, *J. Mater. Sci. Techno.*, 2020, **54**, p 119–131
34. Y.P. Wang, X.R. Zuo, and J.L. Li, Corrosion Resistance of the Welded Joint of Submarine Pipeline Steel with Ferrite Plus Bainite Dual-Phase Microstructure, *Steel Res. Int.*, 2015, **86**, p 1260–1270
35. S. Elbeik, A.C.C. Tseung ,and A.L. Mackay, The Formation of Calcareous Deposits During the Corrosion of Mild Steel in Sea Water, *Corros. Sci.*, 1986, **26**, p 669–680